
Article:
Tsevas, K., Smith, J.A. orcid.org/0000-0001-6889-4408, Kumar, V. et al. (7 more authors) (2021) Controlling PbI2 stoichiometry during synthesis to improve the performance of perovskite photovoltaics. Chemistry of Materials, 33 (2). pp. 554-566. ISSN 0897-4756

https://doi.org/10.1021/acs.chemmater.0c03517

Controlling PbI_2 stoichiometry during synthesis to improve the performance of perovskite photovoltaics

Konstantinos Tsevas[a], Joel A. Smith[b], Vikas Kumar[c], Cornelia Rodenburg[c], Mihalis Fakis,[d] Abd. Rashid bin Mohd Yusoff,[e] Maria Vasilopoulou,[f] David G. Lidzey[b], Mohammad K. Nazeeruddin[g] and Alan D. F. Dunbar[a,]*

[a] Department of Chemical and Biological Engineering, University of Sheffield, Mappin Street, Sheffield S1 3JD, U.K.

[b] Department of Physics & Astronomy, University of Sheffield, Hicks Building, Hounsfield Road, Sheffield, S3 7RH, U.K.

[c] Department of Materials Science and Engineering, University of Sheffield, Mappin Street, Sheffield S1 3JD, U.K.

[d] Department of Physics, University of Patras, 26504, Rio Patras, Greece

[e]Department of Physics, Swansea University, Vivian Tower, Singleton Park, SA2 8PP Swansea, U.K.

[f]Institute of Nanoscience and Nanotechnology, National Centre for Scientific Research Demokritos, 15341 Agia Paraskevi, Attica, Greece

[g]Group for Molecular Engineering of Functional Materials, Institute of Chemical Sciences and Engineering, École Polytechnique Fédérale de Lausanne (EPFL), Rue de l'Industrie 17, CH-1951 Sion, Switzerland.

Corresponding author: a.dunbar@sheffield.ac.uk

Abstract

Over the past decade, remarkable progress has advanced the field of perovskite solar cells to the forefront of thin film solar technologies. The stoichiometry of the perovskite material is of paramount importance as it determines the optoelectronic properties of the absorber and hence the device performance. However, little published work has focused on the synthesis of fully stoichiometric precursor materials of high purity and at high yield. Here, we report a low-cost, energy efficient and solvent-free synthesis of the lead iodide precursor by planetary ball milling. With our synthetic approach we produce low-oxygen, single or multiple polytypic phase PbI_2 with tuneable stoichiometry. We determine the stoichiometry and the polytypes present in our synthesised materials and we further compare them to commercially available materials, using X-ray diffraction, X-ray photoelectron spectroscopy and Rutherford backscattering spectroscopy. Both the stoichiometric PbI_2 we synthesised and a sub-stoichiometric commercially available PbI_2 (where the iodide content is below the optimum Pb:I atomic ratio of 1:2) were used to grow methylammonium lead iodide micro-crystals (which corrects the iodide content). Perovskite solar cells were then produced using stoichiometric and sub-stoichiometric PbI_2 mixed with an equimolar amount of methylammonium iodide and compared to devices produced from re-dissolved microcrystals. The photoactive perovskite layer deposition was processed in air, enabled by the use of a single low-toxicity solvent (dimethyl sulfoxide) combined with vacuum-assisted solvent evaporation. We find that the device performance is strongly dependent upon the stoichiometry of the lead iodide precursor, reaching champion efficiencies over 17 %, with no obvious correlation with its polytypic phases. This work highlights the critical role of PbI_2 stoichiometry in hybrid perovskites, as well as demonstrating synthesis methods and perovskite layer fabrication protocols suitable for low-cost solar energy harvesting.

1. Introduction

Immense academic and commercial research efforts are being undertaken into perovskite solar cells (PSCs), tapping into their potential as the next low-cost solar power technology. The improvement in photovoltaic performance for the most ubiquitous hybrid organic-inorganic halide perovskite absorber (methyl ammonium lead iodide, $CH_3NH_3PbI_3$) has been prodigious, with power conversion efficiencies (PCEs) rising from 3.8 % to 21.2 % in a decade.[1,2] Mixtures of organic and inorganic cations, predominantly methylammonium, formamidinium and caesium ($MA^+/FA^+/Cs^+$) with various halogen anions, such as chloride, bromide and iodide (Cl^-/ Br^-/I^-) have been used to improve the performance and stability of PSC devices. However, the long-term stability and durability of PSCs have remained barriers to their commercialisation. These effects might be related to either deficiency or excess of lead iodide (PbI_2) in the synthesized perovskite, and a tolerance factor closer to unity that corresponds to the cubic crystal structure.[3-7] This degradation occurs regardless of the device architecture utilised (p-i-n or n-i-p).[8] Controlling the stoichiometry of the precursor materials used may help to reduce the presence of impurities and improve the stability of PSC devices. In parallel to the challenge of stability is that of scalability, where the possibility for air processing offers the potentially lowest-cost approach to perovskite fabrication. This necessitates the development of fabrication methods for materials and devices under ambient conditions using less-toxic solvents.

Whilst various researchers have demonstrated the importance of perovskite phase purity and stoichiometry,[9-11] few have covered the role of the precursor materials PbI_2 and methylammonium iodide (CH_3NH_3I),[5,12-14] in particular, the stoichiometry of the PbI_2 and its polytypic behaviour. Previous reports have described more stoichiometrically correct $CH_3NH_3PbI_3$ thin films, synthesised using $CH_3NH_3PbI_3$ single crystals, in comparison with the nominally equimolar intermixed powders of PbI_2 with CH_3NH_3I.[15,16]

PbI_2 is an intrinsic semiconducting material with a wide energy band gap (E_g) of 2.3-2.4 eV.[17] Its crystalline structure, is hexagonally close-packed with the space group $P\bar{3}m1$, consisting of three

alternating layers of lead and iodide atoms (I-Pb-I) within the basic unit cell, which is a near-octahedron $[PbI_6]^{4-}$. For the most stable at room temperature (RT) 2H polytypic phase the unit cell's dimensions are a = b = 0.4557 nm and c = 0.6979 nm.[18] However, the stacking sequence of the $(I\text{-}Pb\text{-}I)_n$ layers can vary significantly, due to the weak Van der Waals interactions between those sequential layers. This results in the crystallochemical phenomenon of polytypism, in which different polytypes with variable c-axis dimensions are formed. These variations in c-axis also result in minor changes to the a- and b-axis.[19-21] Polytype formation can also be dependent on the synthetic process used, for example co-solvent,[22] modified-gel, [23] sublimation, [24] epitaxial [25] or vertical Bridgman-Stockbarger [26] synthesis. During synthesis the formation of multiple polytypic phases may occur. Moreover, reversible and irreversible transitions between different polytypic phases might be responsible for the coexistence of several energy states in the PbI_2,[21,27,28] in a way that is analogous to the polytypism in silicon carbide.[29] Despite the identification of more than 40 polytypic phases of PbI_2 over the last 60 years, primarily using X-ray diffraction techniques, the exact mechanism of their formation and diversity remains poorly understood. Further details regarding the theory of polytypism are provided in SI (Supporting Information) Section 1: Theory of polytypism.

Here, we report the use of a planetary ball milling process (PBM) to synthesise PbI_2, which permits control of the stoichiometry and the degree of polytypism. PBM utilises high kinetic energy, inelastic impacts between stainless-steel spheres surrounded by the reactant powders (lead(II) nitrate and potassium iodide) and the walls of the ball milling jar. This approach provides a controllable and energy efficient way (~ 31.3 watts per hour per gram) to produce moderate quantities at lab scale (≥ 40 grams per run and yield ~ 96 ± 0.5 %) of PbI_2, without using solvents. By avoiding the use of solvent during the PbI_2 synthesis, less waste is produced and a potential route for impurities is removed. We then tested the PSC performance of devices fabricated in air using a single-step deposition method with vacuum assisted evaporation[30,31] of the solvent (dimethyl sulfoxide) and without the use of any additional anti-solvent rinsing step. This fabrication method permits the formation of high-quality

perovskite thin films without using the highly toxic and widely used solvent dimethyl formamide (DMF).[32] PSC devices fabricated using equimolar amounts of sub-stoichiometric PbI_2 and CH_3NH_3I precursors, exhibited inferior performance due to the presence of unreacted PbI_2 in the resultant perovskite thin film. Whereas the polytypic phase of the PbI_2 had no profound effect on the device performance. Our results indicate that the precise control over the stoichiometry of the precursor materials may be a root towards more efficient perovskite solar cells.

2. Results and Discussion

Hydrothermal and mechanochemical synthesis of PbI_2. In order to vary both stoichiometry and polytypism, two methods of synthesis of the PbI_2 have been considered in this work: (1) the conventional hydrothermal (HT) reaction that requires the dissolution of reactants (lead(II) nitrate and potassium iodide) in water and (2) the water-free mechanochemical (MC) process using PBM, which allows the solid state reaction of the same reactants. The HT synthesis of the PbI_2 results in the formation of continuous layers of hexagonal PbI_2 platelets decorated with needle-shaped crystal formations, as shown in Figure 1a. In these needles, incorporation of oxygen was detected by energy dispersive spectroscopy (EDS) point analysis, as can be seen in Table S1. We believe autoionization of water molecules occurs during the HT synthesis of the PbI_2 (Figures 1a and S1a), caused by the strong Coulomb interactions between the ions (Pb^{2+}, K^+, I^- and NO_3^-) and water molecules. That may result in the formation of a mixture of lead oxyiodide and lead iodide hydroxide compounds, with general chemical formulas $Pb(I_{1-x}O_x)_2$ and $Pb(I_{1-y}(OH)_y)_2$, respectively.[33-35]

In contrast, PBM synthesis of PbI_2 causes extensive deformation and fragmentation of the platelets, with reduced particle size (average size < 4 μm), as illustrated in Figures 1b and S1b. No oxygen was detected in the MC powder, as determined by EDS and shown in Table S1, presumably due to the absence of water during the synthesis. Also, for the commercially available PbI_2 powders from Sigma Aldrich with purity 99.999% (SA) and Tokyo Chemical Industries with purity 99.99%

(TCI) the particles (as shown in Figures 1c and 1d, respectively) are considerably larger than the MC sample shown in Figure 1b.

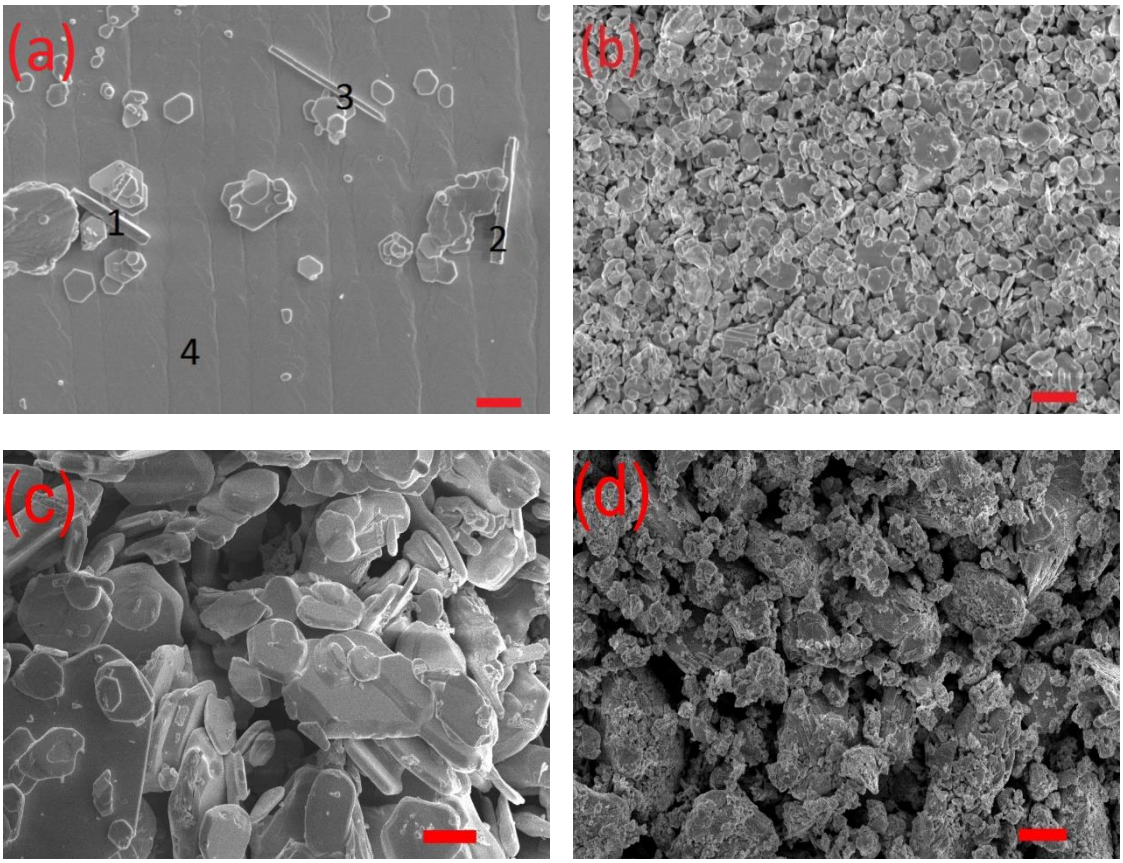

Figure 1. Scanning electron microscopy (SEM) images of lead iodide powders as synthesised by (a) hydrothermal (HT) and (b) mechanochemical (MC) routes, or commercially available from (c) Sigma Aldrich (SA) and (d) Tokyo Chemical Industries (TCI), scale bars represent 10µm. Background and hexagonal shaped formations correspond to PbI_2, while needle shaped crystal formations correspond to oxyiodide and lead iodide hydroxide compounds, in image (a).

PbI_2 powders synthesised by the HT method and the PBM method under three different conditions with respect to the rotation and duration, (MC 1: (200 rpm for 2 hours), MC 2: (400 rpm for 1 hour) and MC 3: (400 rpm for 4 hours), were characterized by X-ray diffraction (XRD), alongside the two commercially available PbI_2 powders, from Sigma Aldrich (SA) and from Tokyo Chemical Industries (TCI), as shown in Figure 2. Differences in the XRD patterns were observed between the mechanochemical (MC 1 to MC 3), HT and commercial SA and TCI materials. The observed XRD peaks were qualitatively labelled based on the corresponding Miller index and the associated polytypic phases. Also, the crystallographic planes and their corresponding Miller indices for each polytypic

phase with respect to the diffraction 2θ angle, are summarized in Table S2. Based on the International Centre for Diffraction Database, XRD peaks of crystallographic planes with Miller indices (001), (011) and (003), correspond to the 2H polytypic phase of PbI_2 with code (01-071-6147) which is the most stable PbI_2 phase at RT, while all the other XRD peaks, correspond mostly to a mixture of 4H (04-017-4470), 14H (04-007-2277) and 20H (04-007-2278) polytypic phases, with characteristic c-axis unit cell dimensions 1.3962 nm, 4.8853 nm and 6.979 nm, respectively. Further quantitative analysis of the polytypic phases present was not possible due to complications associated with overlapping of the XRD peaks that correspond to the 2H with those of 4H, 14H and 20H, respectively. There may also be undetected minor fractions of PbI_2, which have crystallised in a rhombohedral structure.

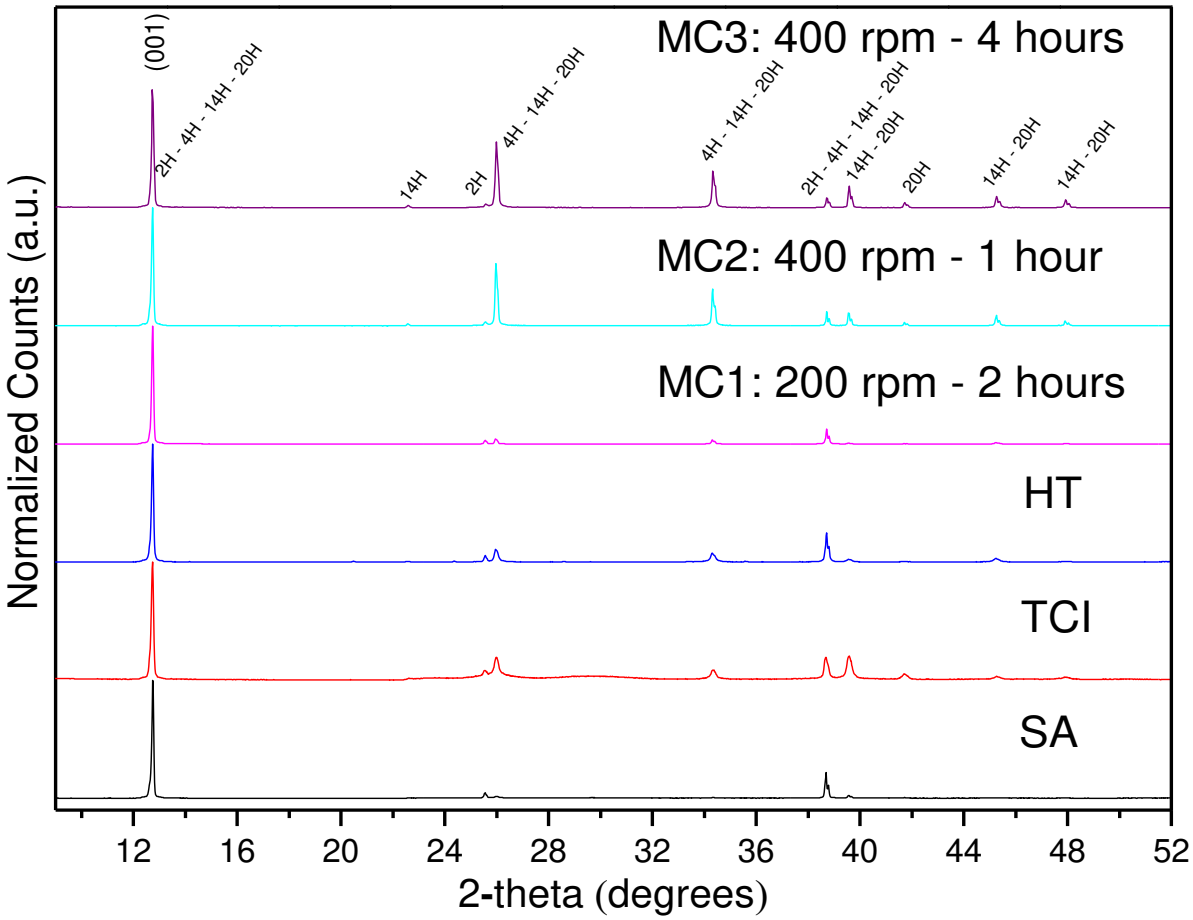

Figure 2. X-ray diffraction (XRD) patterns of commercial (SA and TCI), hydrothermal (HT), and mechanochemical (made under different conditions MC 1, MC 2 and MC 3) PbI_2 powders. Normalization was applied with respect to the intensity of the peak that corresponds to the (001) crystallographic plane for 2H PbI_2. All peaks are labelled based on the polytypic phases 2H, 4H, 14H and 20H which can contribute to scattering at that angle as outlined in Supplementary Information Table S2.

158 The MC 1 sample (200 rpm for 2 hours) did not show strong diffraction at the secondary XRD
159 peak positions, indicating that it has mostly crystallised in a single polytypic phase, closely resembling
160 that of the SA sample. Mechanochemically prepared PbI_2 powders MC 2 and MC 3, show enhanced
161 intensity at the secondary XRD peaks, as a result of the increased rotation speed (400 rpm) and duration
162 (4 hours) of the PBM process. Formation of more than one polytypic phase in the mechanochemical
163 powders (MC 2 and MC 3) make them more comparable with the TCI PbI_2 sample. The presence of
164 additional polytypic phases in MC 2 and MC 3 is attributed to the increased energy given via the
165 inelastic collisions occurring at the higher rotation speed between the stainless-steel spheres
166 surrounded by the reactant powders during the mechanochemical synthesis.

167 **Stoichiometry of the PbI_2 samples.** Three different methods: (1) X-ray photoelectron spectroscopy
168 (XPS), (2) Rutherford back-scattering (RBS) and (3) X-ray diffraction (XRD) studies of perovskite
169 micro-crystals made from the PbI_2, have been utilised to determine the stoichiometry of the PbI_2
170 samples.

171 XPS characterization of the commercial and synthesised PbI_2 samples was conducted to
172 determine the lead to iodide ratio and the amount of oxygen contained in the PbI_2. The stoichiometric
173 variations between the lead and iodide measured and the amount of oxygen are summarised in Table
174 1. It should be noted that these results are averaged values and do not reveal potential localised
175 deviations as a result of polytypism, which may be present in inhomogeneous materials. X-ray induced
176 photolysis of PbI_2 may also occur during the XPS measurement process, therefore, only the general
177 trends in the Pb:I ratio are considered here. Further discussion of inhomogeneity in XPS data and X-
178 ray induced photolysis of PbI_2 is available in SI Section 2: XPS analysis of PbI_2.

179 In the SA material, the lead to iodide ratio was less than the expected 1:2. Whereas for the HT,
180 MC and TCI samples, the ratio varied significantly, with values for (HT, MC 1, MC 3 and TCI) above
181 the stoichiometric 1:2 ratio and for the (MC 2) being almost stoichiometric, as shown in Table 1. This
182 variation in MC samples is attributed to the different conditions used during the PBM process. Rotation

speed was found to be the dominant factor in the process followed by duration.[36] Understanding the influence of using over-stoichiometric (TCI, MC 1 and MC 3) materials as compared to almost stoichiometric MC 2 PbI_2 is of great future research interest. The presence of excess iodide within the perovskite grains or at grain boundaries caused by the use of over-stoichiometric PbI_2,[37] could have detrimental effects on PSCs performance. These may vary with environmental conditions (such as oxygen/inert gas/moisture),[38-39] or diffusion of excess iodide could lead to secondary chemical reactions and degradation of the other incorporated layers in a functioning solar cell device (hole/electron transporting layers or metallic contacts).[40-42]

Table 1. The stoichiometric ratios of different lead iodide samples and their oxygen content percentage from XPS measurements. The samples include commercial (SA and TCI), hydrothermal (HT) and mechanochemically synthesized under different conditions (MC 1 to 3) PbI_2 powders. The data was determined by two high resolution XPS scans (a survey scan followed by high resolution scans were used for all samples).

Lead iodide sample	Synthesis conditions/ sample information	Ratio of Pb:I	Amount of oxygen (%)
MC 3	Mechanochemical (400 rpm 4 hours)	1:2.1 (± 0.1)	2.91 (± 0.01)
MC 2	Mechanochemical (400 rpm 1 hour)	1:2 (± 0.1)	3.97 (± 0.16)
MC 1	Mechanochemical (200 rpm 2 hours)	1:2.1 (± 0.1)	5.21 (± 0.76)
HT	Hydrothermal (in water)	1:2.1 (± 0.1)	7.15 (± 0.21)
TCI	Tokyo Chemical Industries 99.99%	1:2.3 (± 0.1)	4.46 (± 0.14)
SA	Sigma Aldrich 99.999%	1:1.70 (± 0.1)	4.90 (± 0.02)

Rutherford backscattering spectroscopy (RBS) characterization was also conducted to determine the lead to iodide ratio of the commercial and synthesised PbI_2 samples. RBS spectra with normalised yield of lead to iodide in each PbI_2 sample, are shown in Figure S3. Moreover, the extracted stoichiometric ratio between the lead and iodide measured are summarised in Table S3. Uncertainties are given for statistical error, while a 4 % systematic error due to uncertainty in stopping power of the beam of ions was considered. In the SA material, the lead to iodide ratio was 1:1.9 (± 0.008), while in

205 the mechanochemical MC 2 was 1:2.002 (± 0.008). However, for the TCI, MC 1 and MC 3 samples,
206 the ratio shows an excess of iodide to be present.

207 The different PbI_2 materials prepared, shown to have a range of Pb:I ratios and number of
208 polytypic phases as previously discussed, were used to synthesise $CH_3NH_3PbI_3$ micro-crystals. The
209 system of alcohol/PbI_2/CH_3NH_3I, similar to Acik *et al.*,[43] was used to prepare the perovskite micro-
210 crystals which were subsequently characterised by X-ray diffraction (XRD). Two groups of perovskite
211 micro-crystals were prepared as a function of the PbI_2 used and the corresponding amount of CH_3NH_3I,
212 at a range of temperatures (20 ºC, 50 ºC, 70 ºC and 90 ºC). In the first group, the almost stoichiometric
213 MC 2 was reacted either with a) an equimolar amount of CH_3NH_3I, or b) an excess of CH_3NH_3I (30%
214 more CH_3NH_3I by weight), as shown in Figures 3a and 3b, respectively. While, in the second group,
215 sub-stoichiometric SA was reacted either with c) an equimolar amount of CH_3NH_3I, or d) an excess of
216 CH_3NH_3I (30% more CH_3NH_3I by weight), as shown in Figures 3c and 3d, respectively. Each reaction
217 was permitted to proceed for 24 hours at a constant temperature of 20 ºC, 50 ºC, 70 ºC or 90 ºC.

218 Considering the experiments where equimolar amounts of reactants were used to prepare the
219 $CH_3NH_3PbI_3$ micro-crystals, less unreacted PbI_2 was detected when MC2 was used, as compared to
220 SA. The XRD peaks that correspond to the unreacted PbI_2, are identified with asterisks in Figure 3 and
221 are more prevalent in the SA sample (Figure 3 c). The percentage of the unreacted PbI_2 after each
222 reaction at each temperature, was found by integrating the area under the primary XRD peaks and
223 comparing the ratio of (001) PbI_2 to $CH_3NH_3PbI_3$ with Miller indices (002)/(110) that corresponds to
224 the perovskite with tetragonal crystal structure. The results are summarized in Table S4. In contrast,
225 when an excess of CH_3NH_3I was introduced (30 % more CH_3NH_3I by weight) at the most only traces
226 of or zero unreacted PbI_2, was detected in all the $CH_3NH_3PbI_3$ micro-crystals synthesised, regardless
227 of the PbI_2 source (either MC2 or SA), as shown in Figures 3b and 3d, respectively. We believe that
228 methylammonium cations ($CH_3NH_3^+$) and iodide anions (I^-) from the CH_3NH_3I, primarily react with
229 the sub-stoichiometric PbI_2, fulfilling the formation of the $CH_3NH_3PbI_3$ and resulting in some

unreacted PbI_2 (yellow in colour), as shown in Figure S4 during filtering of the $CH_3NH_3PbI_3$ micro-crystals. Consequently, using sub-stoichiometric PbI_2, partially depleted of iodide, during the fabrication of perovskite thin films results in unreacted PbI_2. This could provide a possible explanation for the improved device performance noted in the literature when hydroiodic acid (HI) is used as an additive during the $CH_3NH_3PbI_3$ formation, a correction of the iodide content when the sub-stoichiometric PbI_2 is used, thus reducing under-coordinated Pb.[44]

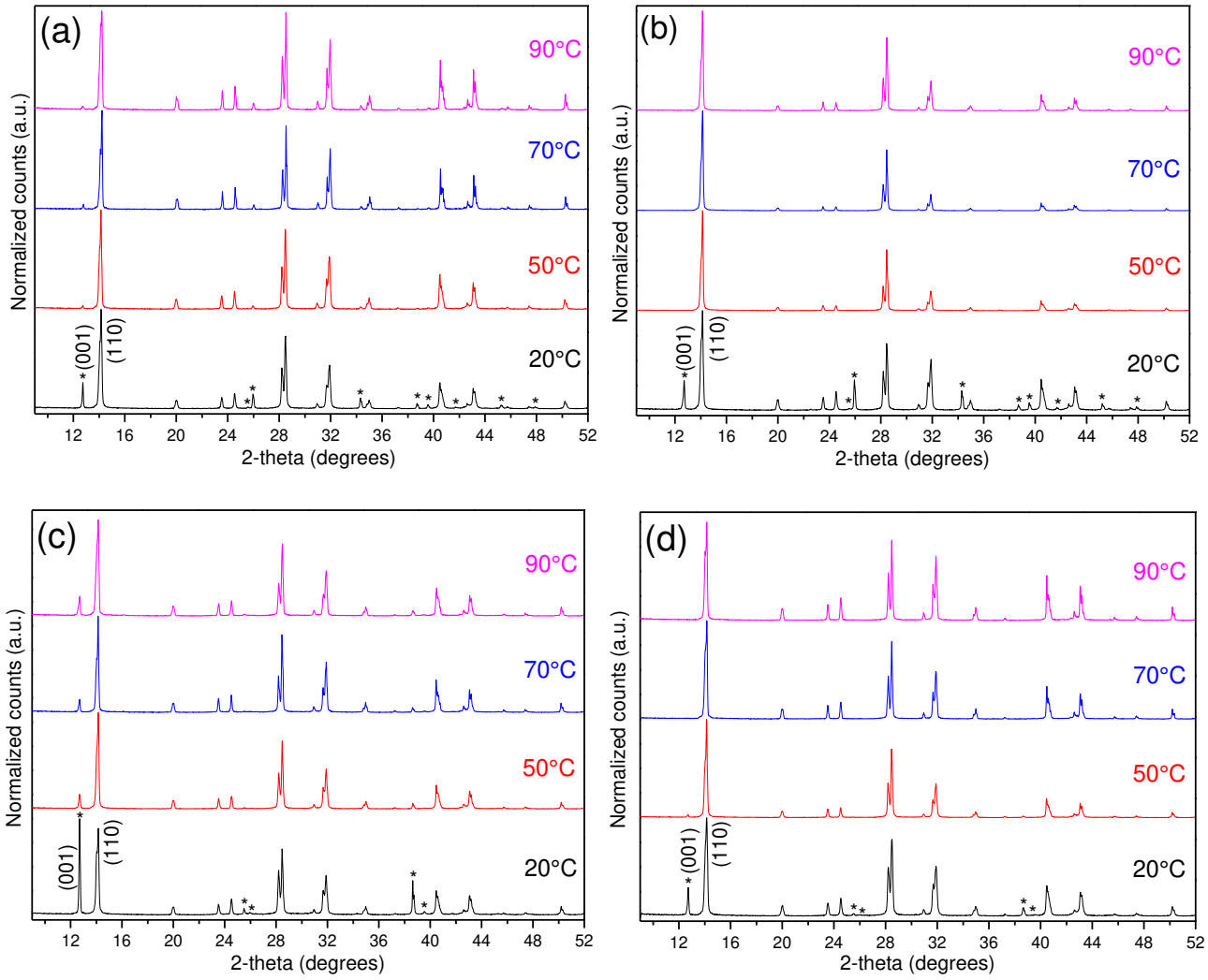

Figure 3. XRD patterns of $CH_3NH_3PbI_3$ micro-crystals synthesised at different temperatures (asterisks represent the XRD peaks of the lead iodide). (a) mechanochemical MC 2 and CH_3NH_3I, with 1 : 1 molar ratio, (b) mechanochemical MC 2 and CH_3NH_3I, with 1:1 molar ratio plus 30 % by weight of CH_3NH_3I, (c) commercial SA and CH_3NH_3I, with 1:1 molar ratio, (d) commercial SA and CH_3NH_3I, with 1:1 molar ratio plus 30 % by weight of CH_3NH_3I. Normalization of XRD patterns was in respect to the peak that corresponds to plane with Miller indices (110) for tetragonal $CH_3NH_3PbI_3$ in all patterns, except for (c) commercial SA and CH_3NH_3I, with 1:1 molar ratio at 20 ºC, which is normalised with respect to the peak of the 2H lead iodide with Miller indices (001).

247 The same system of alcohol/PbI_2/CH_3NH_3I was used to synthesise $CH_3NH_3PbI_3$ micro-crystals
248 with a controlled excess of CH_3NH_3I by weight to determine quantitatively the amount of iodide
249 missing from the PbI_2. These micro-crystal samples were obtained by reacting either sub-
250 stoichiometric SA with 10 %, 15 %, 20 % and 25 % excess of CH_3NH_3I by weight or the almost
251 stoichiometrically correct MC 2 with 2 %, 4 % and 6 % excess CH_3NH_3I by weight, for 24 hours at
252 constant temperature of 90 ºC. The synthesised $CH_3NH_3PbI_3$ micro-crystals were characterised by
253 XRD, as shown in Figures S5. By gradually increasing the amount of excess CH_3NH_3I, the amount of
254 unreacted PbI_2 was reduced, as indicated in the XRD patterns shown in Figures S5a and c. We found
255 that when 20 % excess CH_3NH_3I was reacted with the sub-stoichiometric SA, the weak XRD peak that
256 corresponds to unreacted PbI_2, as shown in Figure S5b, had almost entirely disappeared. This indicates
257 that the required excess of CH_3NH_3I should be slightly greater than 20 % to achieve the complete
258 elimination of unreacted PbI_2 during the synthesis of $CH_3NH_3PbI_3$ micro-crystals when the sub-
259 stoichiometric SA material is used. This value of 20 % excess of CH_3NH_3I by weight is consistent
260 with the value of 10 % excess PbI_2 in the PbI_2/CH_3NH_3I mixture used for the formation of perovskite
261 as reported by Nazeeruddin *et al.*.[45] In both cases the iodine deficiency is corrected, by iodine
262 originating from either the 20 % excess of CH_3NH_3I or the 10 % excess of PbI_2 used, to achieve the
263 required stoichiometry in the final product of $CH_3NH_3PbI_3$. Whereas, when 4 % excess CH_3NH_3I was
264 reacted with the almost stoichiometric MC 2, this resulted in an even weaker PbI_2 XRD peak, as shown
265 in Figure S5d. The stoichiometric ratios for SA and MC 2 were calculated based on the need for either
266 the 20 % more CH_3NH_3I reacting with sub-stoichiometric SA or the 4 % more CH_3NH_3I reacting with
267 the almost stoichiometric MC 2 to eliminate any signal that corresponds to PbI_2 in the XRD data. We
268 found after analysis that the initial (Pb:I) ratio for SA is approximately 1:1.80 and for MC 2 is
269 approximately 1 :1.96, as presented in SI Section 3: Micro-crystal formation to correct the
270 stoichiometry. Also, based on all the above XRD analysis of $CH_3NH_3PbI_3$ micro-crystals, a theory

about the formation of unreacted PbI_2 was developed, as presented in SI Section 4: How iodide deficiency affects perovskite formation, accompanied by several examples, as shown in Table S5.

The results from the XPS and RBS characterization techniques used to determine the lead to iodide ratio in the commercial (SA) and mechanochemical (MC 2) PbI_2 samples, are considered alongside the ratios derived from the synthesis of $CH_3NH_3PbI_3$ micro-crystals with controlled excess CH_3NH_3I and their subsequent XRD characterization (further analysis is provided in SI Section 3: Micro-crystal formation to correct the stoichiometry). The results from all three techniques show consistent trends; less iodide was detected in the SA sample as compared to MC 2 sample, as shown in Figure 4. The large experimental error in the XPS data could be related to X-ray induced photolysis of PbI_2, (further discussion is available in SI Section 2: XPS analysis of PbI_2) and the penetration depth of photons that correspond to X-rays (typically 2-5 nm). Whereas, in RBS with a typical $^4He^+$ ion penetration depth of ~100 nm, the acquired signal might be affected by the number of polytypic phases present and their structural density (2H ρstr.= 6.214 g*cm^{-3}, 4H ρstr.= 5.452 g*cm^{-3}, 14H ρstr.= 6.098 g*cm^{-3} and 20H ρstr.= 6.1 g*cm^{-3}), as provided by the International Centre for Diffraction Database.

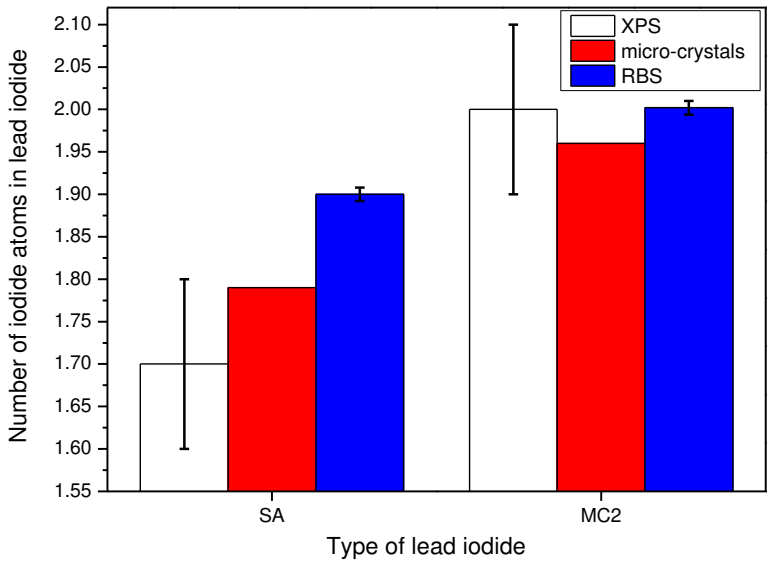

Figure 4. Number of iodide atoms in lead iodide (commercial (SA) and mechanochemical (MC 2)) as function of the characterization technique (XPS correspond to white columns, $CH_3NH_3PbI_3$ micro-crystals correspond to red columns and RBS correspond to blue columns).

290 **Impact of stoichiometry of PbI_2 on device performance**. Fabrication of PSC devices with n-i-p
291 (regular) architecture of glass/ITO/SnO_2/$CH_3NH_3PbI_3$/spiro-OMeTAD/Au was performed, where
292 nanoparticle tin oxide (SnO_2), served as the electron transporting layer (ETL) and spiro-OMeTAD as
293 the hole transporting layer (HTL), to determine how the variable stoichiometry affects the device
294 performance. Comparisons were made between devices fabricated using two varieties of PbI_2. SA,
295 which is depleted in iodide and mechanochemical MC 2 which is almost stoichiometrically correct.
296 PSC devices were made by dissolving either the SA or MC 2 powders with an equimolar amount of
297 CH_3NH_3I in dimethyl sulfoxide (DMSO) to produce photoactive thin films with thicknesses ~550 nm
298 (± 50 nm) and ~380 nm (± 70 nm) as shown in cross-section SEM images Figures S6a and S6b,
299 respectively, after correcting for the 45° sample angle. A second set of PSC devices was also made by
300 re-dissolving $CH_3NH_3PbI_3$ micro-crystals in DMSO. The same two PbI_2 materials (either SA or MC
301 2) were used in reaction with a 30 % excess of CH_3NH_3I by weight. Minor morphological differences
302 of $CH_3NH_3PbI_3$ micro-crystals synthesised at temperature 90 °C, using the two varieties of the PbI_2
303 (either SA or MC 2), are shown in Figures S7a and S7b. The formation of the micro-crystals made
304 with an excess of CH_3NH_3I helped to correct for any deficiency of iodide within the PbI_2. For all the
305 PSC devices, with the photoactive layer made by re-dissolving the $CH_3NH_3PbI_3$ micro-crystals (made
306 using either SA or MC 2) in DMSO, results thin film thicknesses of ~460 nm (± 50 nm) and ~440 nm
307 (± 40 nm), as shown in cross-section SEM images Figures S6c and S6d, respectively, after correcting
308 for the 45° sample angle. The deposition of the photoactive thin films was performed in ambient air
309 and the black/brown perovskite phase formation was accomplished using a vacuum assisted method
310 that promotes the extraction of solvent, in a single step (without an antisolvent rinsing process),[46,47] as
311 shown in Figure S8a (before annealing) and Figure S8b (after annealing), respectively.

312 The average and champion photovoltaic parameters: fill factor (FF), short-circuit current
313 density (J_{SC}), open-circuit voltage (V_{OC}) and power conversion efficiency (PCE)), as measured during

a reverse ($V_{OC} \rightarrow 0$) scan with scan step 10 mVs^{-1}, are illustrated in Figure 5. Additionally, the photovoltaic parameters for all the devices are summarized in Table 3.

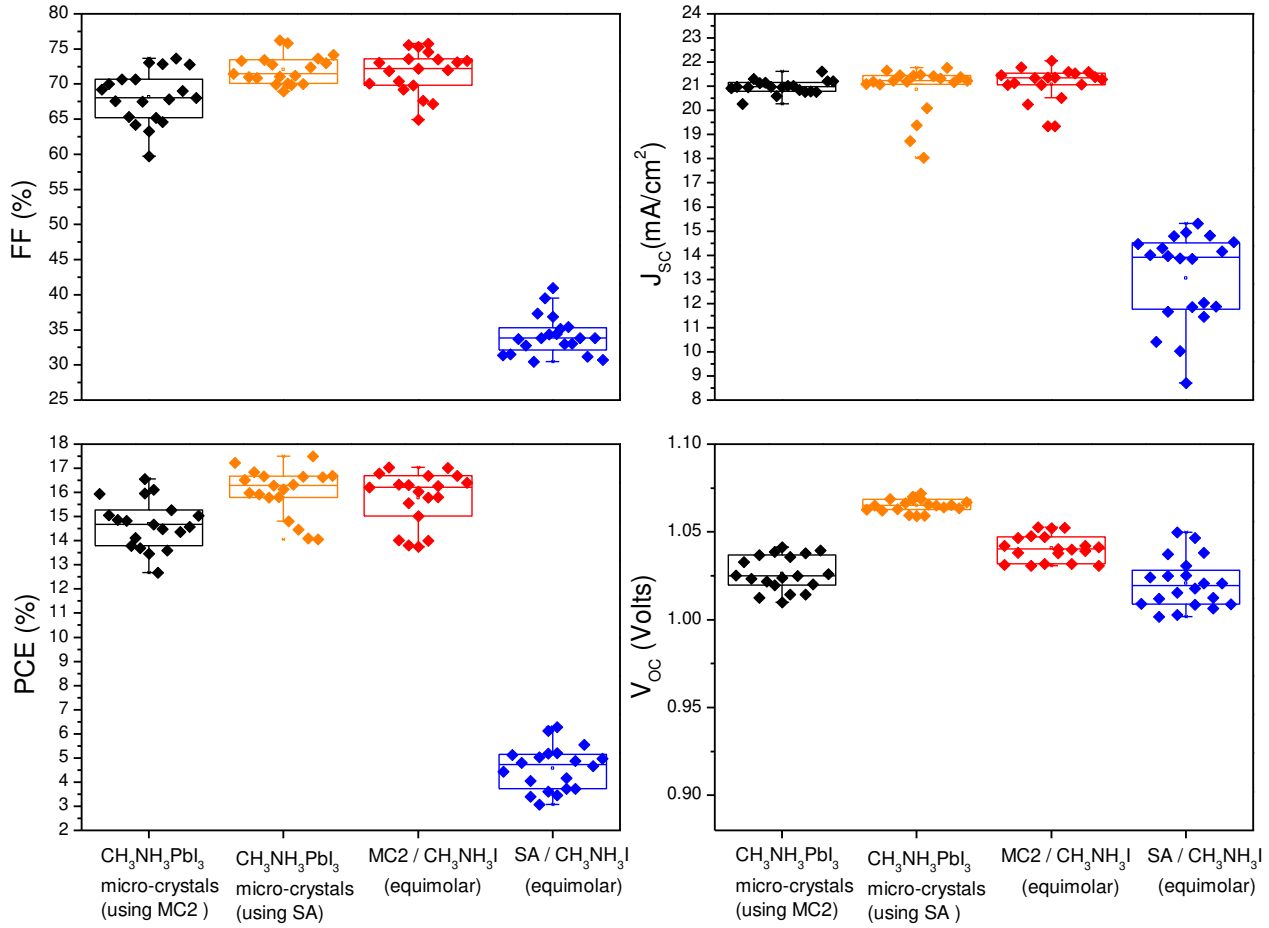

Figure 5. Variation of FF, J_{SC}, PCE and V_{OC} of the solar cell devices as a function of the synthesis route / materials used. Their structure was glass / ITO/SnO_2/$CH_3NH_3PbI_3$ /spiro-OMeTAD/Au. The devices using $CH_3NH_3PbI_3$ micro-crystal synthesis involved a stoichiometry correction step for iodide by the addition of CH_3NH_3I. The devices using equimolar amounts of PbI_2 and CH_3NH_3I powders, did not include this step.

329 **Table 3**: The performance parameters of solar cell devices with the structure glass
330 ITO/SnO_2/$CH_3NH_3PbI_3$/spiro-OMeTAD/Au, as a function of the starting materials used and the
331 synthesised $CH_3NH_3PbI_3$ micro-crystals. The photovoltaic parameters of the average values from 20
332 devices in bold and champion devices in parenthesis.
333

		FF (%)	**J_{SC} (mA/cm^2)**	**V_{OC} (Volts)**	**PCE (%)**
Dissolution of $CH_3NH_3PbI_3$ micro-crystals in DMSO	$CH_3NH_3PbI_3$ micro-crystals (synthesised using MC 2)	**68.19** (73.66)	**20.98** (21.61)	**1.03** (1.04)	**14.69** (16.55)
	$CH_3NH_3PbI_3$ micro-crystals (synthesised using SA)	**72.08** (75.82)	**20.87** (21.65)	**1.06** (1.06)	**16.02** (17.40)
Dissolution of equimolar PbI_2 / CH_3NH_3I in DMSO	MC 2/CH_3NH_3I (equimolar)	**71.75** (75.29)	**21.09** (21.60)	**1.04** (1.05)	**15.77** (17.07)
	SA/CH_3NH_3I (equimolar)	**34.18** (41.01)	**13.06** (14.96)	**1.02** (1.02)	**4.58** (6.26)

334

335 Notably, the photovoltaic parameters are significantly enhanced in PSC devices made from
336 either $CH_3NH_3PbI_3$ micro-crystals, where the iodide content was corrected by the processing regardless
337 of the number of polytypic phases in the PbI_2 used (SA or MC2), or when equimolar amounts of almost
338 stoichiometric MC 2 with CH_3NH_3I were used. In comparison, the device performance parameters
339 (FF, J_{SC} and PCE) of PSC devices fabricated using equimolar amounts of the SA with CH_3NH_3I, were
340 notably inferior. This reduction in device performance is attributed to the presence of a significant
341 amount of unreacted PbI_2 between, covering or possibly within the grains of the $CH_3NH_3PbI_3$.[48-50]
342 Also, the characteristic current density–voltage (J-V) curves in forward ($0 \rightarrow V_{OC}$) and reverse (V_{OC}
343 $\rightarrow 0$) scans of PSC devices, were compared as a function of the photoactive layer fabricated using
344 either $CH_3NH_3PbI_3$ micro-crystals or equimolar amounts of different PbI_2 with CH_3NH_3I, are shown
345 in Figure S9. In all the plots, black curves correspond to the average from all J-V curves recorded and
346 the error bars represent the deviation across all the devices. Hysteresis was observed between the J-V
347 curves for the forward ($0 \rightarrow V_{OC}$) and reverse ($V_{OC} \rightarrow 0$) scans for all devices, and of the higher
348 performing conditions was worst in the case for the equimolar of reactants used. All the J-V curves

349 (either in reverse or forward scans) of PSC devices fabricated using equimolar amounts of the sub-
350 stoichiometric PbI_2 (SA) with CH_3NH_3I were notably inferior in performance, as shown in Figure S9d.
351 Less hysteresis was observed between forward and reverse scans of PSC devices fabricated using
352 equimolar amounts of the sub-stoichiometric PbI_2 (SA) with CH_3NH_3I. The hysteresis could be related
353 to ion migration originating from unreacted PbI_2 likely present between the grain boundaries, and also
354 possibly within the grains themselves, affecting the diffusion lengths of charge carriers. It may be
355 masked in the SA sample because of the considerably lower current observed. We believe the amount
356 of iodide present in the sub-stoichiometric SA is insufficient to form the exact composition of
357 $CH_3NH_3PbI_3$, but this can be corrected by using the above method for the preparation of micro-crystals
358 to adjust the stoichiometry.

359 In order to shed light on the differences in the device performance, the internal photon-to-
360 electron-conversion efficiencies (IPCE) of the fabricated PSC devices were measured. The results are
361 shown in Figure 6a and clearly demonstrate that the photon-to-electron conversion process is more
362 efficient for the devices based on perovskite absorbers synthesized from the close to perfectly
363 stoichiometric precursors. Furthermore, electron-only devices with the structure
364 FTO/SnO_2/$CH_3NH_3PbI_3$/PCBM/Ag were fabricated and their J-V characteristics were measured under
365 dark conditions, as shown in Figure 6b. These results indicate that the electron injection is inferior in
366 the device when the sub-stoichiometric PbI_2 with an equimolar amount of CH_3NH_3I were used. This
367 can be explained by the presence of a large excess of unreacted PbI_2 within the perovskite synthesized
368 from the sub-stoichiometric precursor material.

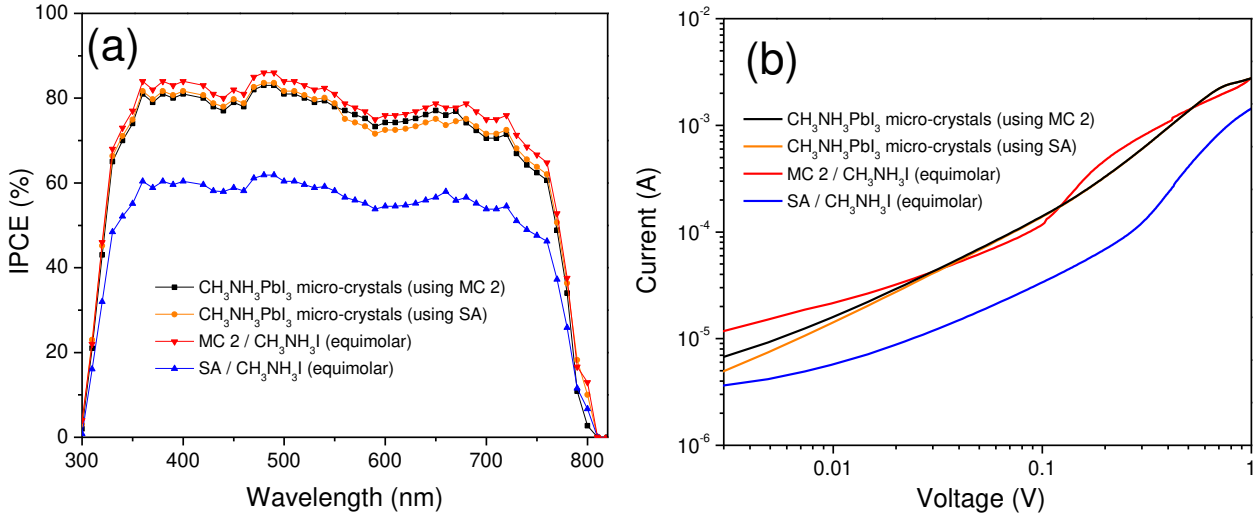

Figure 6. (a) IPCE and (b) electron current of perovskite solar cells and electron-only devices, respectively, using, $CH_3NH_3PbI_3$ micro-crystals (using MC 2) (black curves), $CH_3NH_3PbI_3$ micro-crystals (using SA) (orange curves), equimolar amounts of MC 2/CH_3NH_3I (red curves), equimolar amounts of SA/CH_3NH_3I (blue curves).

The presence of unreacted PbI_2 in the perovskite films obtained when using equimolar amounts of SA/CH_3NH_3I was also confirmed by the short wavelength shoulder present in the visible infrared (Vis-IR) absorption spectra shown in Figure 7a. The experimentally calculated optical band gap values (E_{obg}) for the PbI_2 (E_{obg}= 2.53 eV (± 0.01 eV) and $CH_3NH_3PbI_3$ (E_{obg}= 1.48 eV), as determined by Tauc plots, support the hypothesis that unreacted PbI_2 might also form within the perovskite grains because they show a deviation from the optical band gap values that correspond to the neat PbI_2 (E_{obg}= 2.36 eV) and the $CH_3NH_3PbI_3$ (E_{obg}= 1.51 eV),[51] as presented in Figures S10a and S10b, respectively. Also, the presence of unreacted PbI_2 in the perovskite films obtained when equimolar amounts of SA and CH_3NH_3I were used, results in a binary mixture of $CH_3NH_3PbI_3$ and PbI_2 (with $CH_3NH_3PbI_3$ as the major phase and PbI_2 as a minor phase) with E_{obg}= 1.48 eV, and a similar binary mixture (with PbI_2 as the major phase and $CH_3NH_3PbI_3$ as the minor phase) with E_{obg}= 2.53 eV (± 0.01 eV). Consequently, when equimolar amounts of SA and CH_3NH_3I are used, formation of those binary mixtures which are neither pure $CH_3NH_3PbI_3$ nor pure PbI_2, may lead to materials with absorption coefficients different than their absolute values.[52] Wang *et al.*, and Cui *et al.* reported that different

precursor ratios of PbI_2:CH_3NH_3I affects the optoelectronic properties of the resulting $CH_3NH_3PbI_3$ formed, such as the Fermi level, charge carrier mobilities, carrier concentrations and recombination rates.[53,54] Further details of how this can result in unreacted PbI_2 in the resulting perovskite film are given in SI Section 4. Steady-state photoluminescence (PL) spectra of the different perovskite samples deposited on SnO_2/ITO substrates were also measured (Figure 7b). The PL intensities varied significantly and were much lower for the perovskite films fabricated from the stoichiometric precursors or for those where the stoichiometry has been adjusted through processing (micro-crystals). While it is difficult to disentangle the effects of interface recombination and carrier extraction, this difference could be due to either fewer defects in the samples fabricated using micro-crystals or efficient blocking in samples based on the presence of unreacted PbI_2. However, in light of the PSC device data, we attribute this difference to suppressed electron injection into the ETL in the SA/ CH_3NH_3I sample leading to increased bulk radiative recombination. Upon perovskite photoexcitation in the SnO_2/perovskite samples, electrons are transferred from its conduction band (lying at about -3.9 eV) to the lower conduction band of SnO_2 (lying about -4.1 eV) hence suppressing the PL signal. In the PbI_2 rich samples this electron transfer pathway is blocked due to the insulating properties of PbI_2.

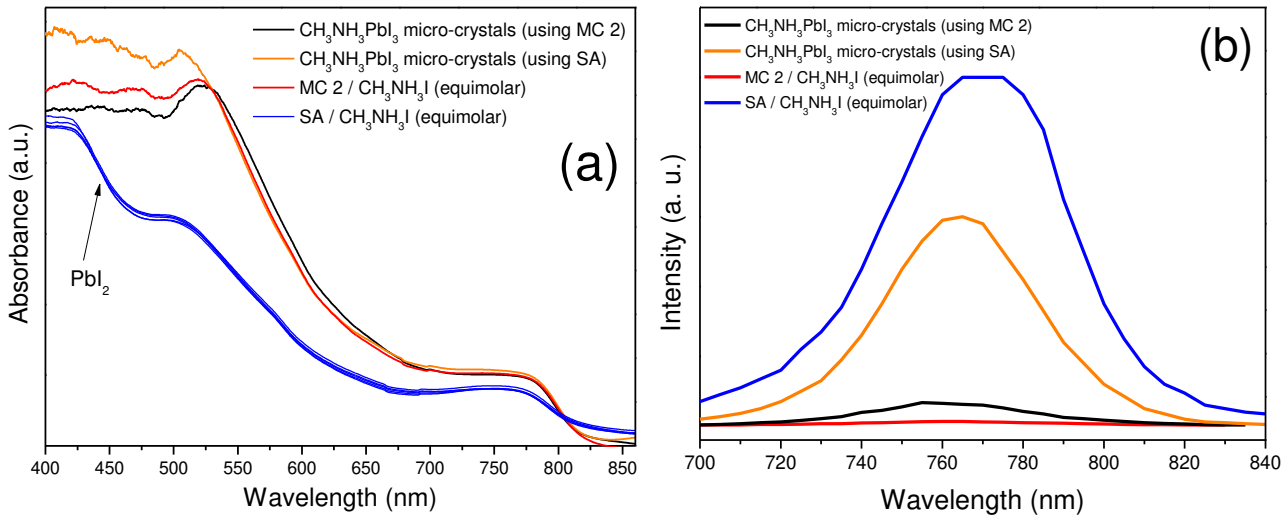

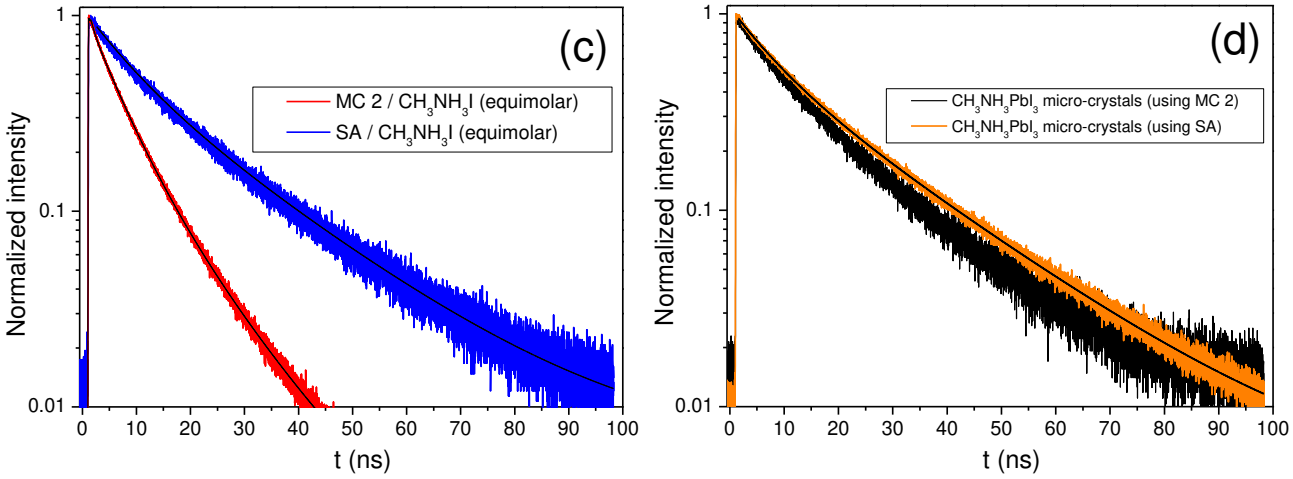

Figure 7. (a) Visible-infrared (Vis-IR) absorbance, (b) steady-state photoluminescence (PL) spectra, (c) and (d) TRPL decay curves of perovskite thin films synthesised using, $CH_3NH_3PbI_3$ micro-crystals (using MC 2) (black curves), $CH_3NH_3PbI_3$ micro-crystals (using SA) (orange curves), equimolar amounts of MC 2/CH_3NH_3I (red curves), equimolar amounts of SA/CH_3NH_3I (blue curves) (from five different measured points only in figure (a). Absorbance due to the presence of unreacted lead iodide is indicated with black arrow in figure (a).

This was further corroborated by the transient PL (TRPL) measurements taken on the same samples (detection at 770 nm) (Figure 7c and d and Table S6) which indicated faster electron transfer from the excited perovskite towards the SnO_2 in the equimolar MC 2/CH_3NH_3I sample compared to the SA/CH_3NH_3I counterpart. We note that the small difference in the decay kinetics between equimolar and micro-crystal samples may be due to the differences in morphology.

The above results indicate that the perovskite samples derived from sub-stoichiometric precursors are enriched in insulating PbI_2, which is may formed between the grains or combined within consecutive layers of ($CH_3NH_3PbI_3$/PbI_2) likely formed within the grains of the $CH_3NH_3PbI_3$.[55] The formation of $CH_3NH_3PbI_3$ ferroelastic domains, regardless of the stoichiometry in PbI_2, has also been noted in literature [55-57] and is confirmed here by AFM (Figure S11). This phenomenon may also explain the spatial variability of the J_{SC} within individual $CH_3NH_3PbI_3$ grains, as reported by Kutes *et al.*.[58] The measured roughness of all fabricated $CH_3NH_3PbI_3$ thin films using the vacuum assisted method was less than 16 nm, as measured by AFM. Also, an increased concentration of larger pinholes formed in the $CH_3NH_3PbI_3$ thin films fabricated from the $CH_3NH_3PbI_3$ micro-crystals regardless of the PbI_2

426 used (either sub-stoichiometric SA or almost stoichiometric MC2) as observed in LV-SEM images
427 Figures S12a and S12b. This might suggest that with further process development, such as by further
428 modifying the 1.13 M concentration of the perovskite ink using the $CH_3NH_3PbI_3$ micro-crystals, even
429 better photovoltaic performance is achievable by this route. For all the LV-SEM images in Figure S12,
430 grain size distribution calculations were conducted and are summarized in Figure S13. Specifically,
431 the majority of grains on $CH_3NH_3PbI_3$ thin films when micro-crystals were employed and fabricated
432 using the almost stoichiometric MC 2 PbI_2 had an average size of 110 ± 10 nm. Whereas the majority
433 of grains had an average size of 90 ± 10 nm when micro-crystals were prepared using the sub-
434 stoichiometric SA PbI_2. Also, equimolar amounts of the almost stoichiometric MC 2 PbI_2/CH_3NH_3I
435 resulted in thin films with the maximum average grain size of 175 ± 25 nm. While, for thin films of
436 perovskite made using equimolar amounts of sub-stoichiometric SA PbI_2/CH_3NH_3I the average grain
437 size was 130 ± 10 nm. The smaller grain sizes observed when using the micro-crystal processing route
438 may be due to slightly different growth mechanisms occurring in the perovskite thin films made from
439 $CH_3NH_3PbI_3$ micro-crystals and equimolar amounts of reactants, which requires further investigation.
440

441 ## 3. Conclusion

442 In conclusion, planetary ball milling is a low-cost, energy efficient pathway to produce PbI_2 with
443 reduced oxygen content, whereby it is possible to control both the stoichiometry and polytype of the
444 resulting PbI_2 by varying the mechanochemical parameters of synthesis (revolutions per minute and
445 duration). The absence of water during the PbI_2 production via planetary ball milling allows for a
446 significant reduction in the oxygen content present as determined by XPS analysis. Although the
447 polytypism of PbI_2 precursor had no profound effect on the solar cell performance, its stoichiometry
448 was proven to exhibit serious implications for the device performances. PSC devices with a
449 photoactive layer manufactured using sub-stoichiometric PbI_2 showed reduced performance due to the
450 large excess of PbI_2 in the perovskite film, unless an excess of CH_3NH_3I was used via the fabrication

of $CH_3NH_3PbI_3$ micro-crystals. If the PbI_2 was stoichiometrically correct, an excess of CH_3NH_3I was not necessary. Using stoichiometrically corrected PbI_2, in combination with the single step vacuum assisted method which is free of any antisolvent rinse step and does not use other toxic solvents, promotes the formation of $CH_3NH_3PbI_3$ with close to no detectable unreacted PbI_2. This processing route can help enable a low-cost and air-processable fabrication route for PSC devices with repeatably high performance. This work highlights the importance of proper material control and synthesis procedures to achieve enhanced quality of PSC devices.

4. Experimental Details

Methylammonium iodide synthesis. Methylammonium iodide (CH_3NH_3I), was synthesised by adding dropwise 38 mL of hydroiodic acid (57 % w / w in water, Alfa Aesar) in 30 mL of methylamine (40 % w / w in water, Sigma Aldrich), in a 250 mL round bottom flask at 0 °C (ice bath) and constantly stirring (400 rpm) for 2 hours. The round bottom flask was transferred into an oil bath at a temperature of 90 °C, to evaporate off the water for 6-7 hours. The resulting yellow/white precipitate was further purified by recrystalising two times from pure anhydrous ethanol. The white / transparent crystallised flakes were collected by vacuum filtration (Whatman filter paper grade 5 with pore size 2.5 μm) and dried in a vacuum oven at 50 °C for 24 hours, before storage in dark conditions. The same methylammonium iodide, was used for both the synthesis of the $CH_3NH_3PbI_3$ micro-crystals and perovskite solutions.

Hydrothermal PbI_2 synthesis. Hydrothermal PbI_2, was synthesised by dissolving 1 g of lead (II) nitrate ($Pb(NO_3)_2$, Sigma Aldrich) with purity ≥ 99 % and 1.01 g of potassium iodide (KI, Honeywell Fluka) with purity ≥ 99 % (both precursors as received) in a 1 L volume round bottom flask filled with

476 1 L of boiled (100 °C) ultra-pure deionised water (Sigma Aldrich) with resistivity 18.2 MΩ. The round
477 bottom flask was covered with towel made of fibre glass and left to cool down slowly to room
478 temperature for 24 hours. An excess of potassium iodide was used, to complete the reaction of the
479 $Pb(NO_3)_2$, based on the chemical reaction: $Pb(NO_3)_2 + 2KI \rightarrow PbI_2 + 2KNO_3$. The golden coloured
480 crystalline flakes of PbI_2, were collected after vacuum filtration (Whatman filter paper grade 5 with
481 pore size 2.5 μm) and dried in a vacuum oven at 50 °C for 24 hours, before further characterisation.
482 **Mechanochemical PbI_2 synthesis**. Mechanochemical PbI_2 powder, was synthesised using a planetary
483 ball milling machine (PM 100 Retsch) at variable revolutions per minute and time duration. 30 g of
484 $Pb(NO_3)_2$ with purity ≥ 99 %, 30.07 g of KI with purity ≥ 99 % and 160 stainless - steel spheres of
485 diameter 6 mm, were mixed in a ball milling jar of capacity 500 mL. Oxygen reduction inside the ball
486 milling jar was conducted by displacing the air, with argon gas of purity 99 %. This oxygen reduction
487 was only applied for the mechanochemical sample MC 3 (400 rpm 4 hours), leading to oxygen
488 reduction by ~ 36 (± 10) %, in comparison with the mechanochemical samples MC 1 / MC 2
489 synthesised without the introduction of argon gas. We expect, further oxygen reduction in the
490 mechanochemical PbI_2 powders, might be achievable by careful drying the reactants used and by
491 displacing the air with ultra-pure argon gas (> 99.99 %) inside the ball milling jar. The yellow coloured
492 PbI_2 powder was separated from the stainless-steel spheres and washed 5 times with 70 - 80 mL (each
493 time) of deionised water during vacuum filtration (Whatman filter paper grade 5 with pore size 2.5
494 μm), to remove any potassium nitrate by-product. Finally, the PbI_2 was dried in a vacuum oven at 50
495 °C for 24 hours, before storage in dark conditions and further characterisation. The yield of the
496 produced PbI_2 (MC 2) was defined by the relative number of product / reactant moles, between the
497 PbI_2 and the $Pb(NO_3)_2$ (considering as ideal molecular weight for the PbI_2, to be 461.01 g / mol),
498 resulting $((40.32\ g / 461.01\ g * mol^{-1}) / (30\ g / (331.21\ g * mol^{-1})) * 100\ \% \approx 96.5\ \%$.
499 **$CH_3NH_3PbI_3$ micro - crystals synthesis**. $CH_3NH_3PbI_3$ micro-crystals, were synthesised by reacting
500 0.7 g of the almost stoichiometric MC 2 or sub-stoichiometric SA PbI_2 (used as received and stored in

501 dark conditions) with an equimolar amount of CH_3NH_3I (0.2414 g) or an equimolar amount plus 30 %
502 excess by weight of CH_3NH_3I (0.2414 g + 0.0724 g = 0.3138 g), in 15 mL of 1-pentanol at variable
503 temperatures (20 °C, 50 °C, 70 °C and 90 °C) for 24 hours (in oil bath). In this process, 1-pentanol
504 which is a polar protic non-toxic alcohol, was used to selectively dissolve only the methylammonium
505 iodide, but not the PbI_2 powder and the final product of the $CH_3NH_3PbI_3$ micro-crystals. Black powder
506 of $CH_3NH_3PbI_3$ micro-crystals, was collected by vacuum filtration (Whatman filter paper grade 5 with
507 pore size 2.5 μm) and washed with 5 mL of chlorobenzene (Alfa Aesar) during the filtration step,
508 followed by drying in a vacuum oven for 30 min at room temperature, before further characterisation.
509 After completion of the chemical reaction the 1 - pentanol / PbI_2 / CH_3NH_3I solution must be kept
510 warm and filtrated as fast as possible (< 2 sec). Recrystallization of the excess CH_3NH_3I dissolved in
511 the 1 – pentanol during the vacuum filtration process (to separate out the $CH_3NH_3PbI_3$ micro-crystals)
512 was prevented by the use of a large volume of 1-pentanol, which reduces the probability of the
513 dissolved ions ($CH_3NH_3^+$ and I^-) interacting. Unreacted $CH_3NH_3^+$ and I^- ions remain dissolved in the
514 warm 1-pentanol and are therefore removed from the micro-crystals upon filtration.
515 **Dry dimethyl sulfoxide preparation**. Dry dimethyl sulfoxide (DMSO, Sigma Aldrich), was prepared
516 by intermixing 150 mL of as received dimethyl sulfoxide (DMSO) with purity ≥ 99.5 % and 20 g of
517 magnesium sulfate ($MgSO_4$, Fisher Chemical) in a 250 mL round bottom flask. The round bottom
518 flask was capped and left in a fume hood at room temperature for at least two weeks before extracting
519 crystal clear dry DMSO.
520 **Perovskite solution preparations**. Perovskite solutions were prepared, either by dissolving 0.4 g of
521 the almost stoichiometric MC 2 or sub-stoichiometric SA PbI_2, directly with an equimolar amount of
522 CH_3NH_3I (0.1379 g) in 0.620 mL of dry DMSO, with a final concentration of 2.8 M or by dissolving
523 0.4 g of the $CH_3NH_3PbI_3$ micro-crystals synthesised using the almost stoichiometric MC 2 or sub-
524 stoichiometric SA PbI_2 in 0.571 mL of dry DMSO with a final concentration of 1.13 M. Additionally,
525 all perovskite solutions were kept on a hot plate at a temperature of 100 °C for 10 min, to ensure

526 complete dissolution of the reactants in DMSO, before being filtered through a PTFE filter (pore size
527 0.45 μm) and kept under constant stirring (~ 300 rpm) and temperature (65-70 °C) in a custom-made
528 aluminium block, see Figure S14, before deposition. The block helped to reduce condensation of the
529 DMSO on the inside of the vial walls, thereby preventing premature perovskite crystallisation. In all
530 our experiments with $CH_3NH_3PbI_3$ micro-crystals, the solution concentrations were calculated based
531 on the assumption of perfect $CH_3NH_3PbI_3$ micro-crystals with molecular weight 619.98 g mol^{-1}, as
532 defined by the atomic mass units of each element in the $CH_3NH_3PbI_3$ and prepared 24 hours, after their
533 synthesis. Also, in all our experiments with either commercial SA or mechanochemical MC 2, solution
534 concentrations were calculated based on the false assumption of stoichiometrically perfect PbI_2 (Pb :
535 I = 1 : 2, atoms ratio), with molecular weight 461.01 g * mol^{-1}.
536 **Device fabrication**. Glass substrates pre-patterned with six ITO (indium tin oxide) pixels (20 Ω /
537 square, Ossila) were first sonicated for 10 min in a solution made of 1 mL detergent (Hellmanex (III))
538 and 250 mL boiled deionised water (100 °C). Any residual detergent was subsequently washed off by
539 rinsing the substrates three times with 100 mL (each time) of deionised water. The Glass / ITO
540 substrates, were further sonicated two more times for 10 min (each time) in 250 mL acetone and then
541 250 mL isopropanol. The cleaned substrates were then treated with oxygen plasma for 10 min to
542 remove organic contaminants. Clean glass / ITO substrates were transferred into a cleanroom (class
543 1000) with constant temperature 20 °C and humidity 30 %, for deposition of the electron transporting
544 layer and perovskite thin film. A colloidal dispersion of tin (IV) oxide (SnO_2) in deionised water (15
545 %, Alfa Aesar), was spin coated at 3000 rpm for 30 s, followed by removal of the SnO_2 from part of
546 the substrate using a cotton bud, re - exposing the ~ 4 - 5 mm ITO electrode. The coated substrates
547 were then annealed at 150 °C for 30 min and cooled down to 20 °C, without any further treatment.[59]
548 50 μL of the perovskite solutions made of either $CH_3NH_3PbI_3$ micro-crystals in DMSO with
549 concentration 1.13M or solutions of (almost stoichiometric MC 2 or sub-stoichiometric SA) PbI_2
550 reacted with equimolar amount of CH_3NH_3I in DMSO with concentration 2.8M, were statically

551 dispersed onto the glass / ITO / SnO_2 samples followed by spin coating at 2500 rpm or 3100 rpm for
552 10 s, respectively. Each substrate was placed in a custom-made vacuum chamber for 120 s and pressure
553 ~ 0.02 mbar, as shown in Figure S15. Then each substrate was annealed on a hot plate at 100 °C for
554 30 s. All glass/ITO/SnO_2/$CH_3NH_3PbI_3$ samples were then transferred inside a nitrogen filled glove box
555 for the synthesis and deposition of doped hole transporting layer of 2,2',7,7'-Tetrakis [*N,N*-di (4-
556 methoxyphenyl) amino]-9,9'-spirobifluorene (spiro-OMeTAD ≥ 99.5 %, Ossila). The 86.6 mg of
557 spiro-OMeTAD powder was dissolved in 1 mL of chlorobenzene. The solution was then doped with
558 lithium bis(trifluoromethanesulfonyl)imide (Li-TFSI ≥ 99 %, Sigma Aldrich), 4-*tert*-butylpyridine
559 (TBP 96.6 %, Sigma Aldrich) and FK209 (FK 209 Co(II) PF6, Greatcell). The quantity of dopants
560 used in 1 mL of the spiro-OMeTAD / chlorobenzene solution was as follows, 20 µL of Li-TFSI (500
561 mg * mL^{-1} in acetonitrile), 34 µL of TBP and 11 µL of FK209 (300 mg * mL^{-1} in acetonitrile). The
562 solution was filtered with a PTFE filter (pore size 0.2 µm) and then 50 µL was spin coated on each
563 sample dynamically at 4000 rpm for 30 s. Devices were left overnight in dry air to allow for the spiro-
564 OMeTAD to be oxidised. Finally, 80 nm of gold was deposited in an Edwards thermal evaporator,
565 with a deposition rate 0.1 Å s^{-1} for the first 2 nm and then 1 Å s^{-1} for the remaining thickness.[60] All un
566 - encapsulated PSCs devices were immediately characterised electrically.

567 **Photocurrent density-voltage (J-V) measurements**. Photocurrent density-voltage (J-V)
568 characteristics were measured under AM 1.5G light (1000 W m^{-2}) produced by a xenon lamp (Newport
569 solar simulator). The light intensity was calibrated using a silicon reference cell (Newport). Each solar
570 cell device was mounted and covered with a six-pixelated cell shadow mask, with aperture area of
571 0.0256 cm^2 per cell. Cells were scanned from -0.2 V to 1.2 V and then back to -0.2 V at a scan step of
572 0.01 V * s^{-1} using a Keithley 237 source measure unit.

573 **Powder X-ray diffraction measurements**. X-ray diffraction patterns of all (commercial (used as
574 received and stored in dark conditions), hydrothermal and mechanochemical) lead iodide powders and
575 $CH_3NH_3PbI_3$ micro-crystals, were obtained using a D2 Phaser (Bruker) diffractometer under

576 monochromatic Cu Kα radiation (λ = 1.54184 Å) and step size 2θ = 0.020273 degrees over the 2θ
577 range from 9º to 52º. X-ray diffraction patterns of $CH_3NH_3PbI_3$ micro-crystals with different amount
578 of excess CH_3NH_3I, were obtained at double acquisition time for higher accuracy. Also, all
579 measurements of powders were taken using a zero-background holder made of monocrystalline silicon.
580 **SEM images and EDS analysis**. Scanning electron microscopy (SEM) images and energy dispersive
581 spectroscopy (point or full image) elemental analysis, were obtained using a JSM-6010LA (JEOL) at
582 accelerating voltages 12 kV and 15 kV, respectively. Low voltage scanning electron microscope
583 images, were obtained using a FEI Helios NanoLab G3 UC SEM at accelerating voltage 2 kV using a
584 through-lens detector (TLD) at working distance of 4.2 mm and with beam current of 13 pA.
585 **Visible – infrared (Vis-IR) spectroscopy measurements**. Absorption spectra of all $CH_3NH_3PbI_3$ thin
586 films, were obtained using a spectrometer (USB2000 + UV-VIS-ES) equipped with a deuterium
587 halogen light source (UV-VIS-NIR_DT-MINI-2-GS), both from Ocean optics.
588 **Time-resolved photoluminescence (TRPL) measurements.** The time-resolved photoluminescence
589 measurements were performed using the Time-Correlated Single Photon Counting (TCSPC) method
590 (FluoTime 200, Picoquant) under magic angle conditions. Excitation was performed by a pulsed diode
591 laser at 470 nm and the instrument's response function (IRF) was ~ 80 ps. Multi-exponential functions
592 convoluted with the IRF were used for the fitting taking into account that the χ^2 factor should be smaller
593 than 1.1.
594 **X-ray photoelectron spectroscopy (XPS) measurements**. Each powder was mounted for analysis by
595 pushing the powder into indium foil. The indium foil was then mounted directly onto the sample holder
596 using double sided conducting carbon tape. The analyses, were carried out using a Kratos Supra
597 instrument with a monochromatic aluminium source and energy 1486.69 eV. Survey scans, were
598 collected between binding energies from 1200 to 0 eV, at 1 eV intervals with an acquisition time of 10
599 min. (per point) from two analysis points per sample. High resolution scans, were also collected for
600 the I 3d, O 1s, C 1s and Pb 4f core levels, at 0.1 eV intervals with an acquisition time of 5 min, for

601 each point. The data collected, were calibrated in intensity using a transmission function characteristic
602 of the instrument to make the values instrument independent. The data was then quantified using the
603 CasaXPS software, determining the transmission functions as provided by National Physical
604 Laboratory (NPL). Binding energy calibrations for all survey or high-resolution scans, were conducted
605 with respect to the Pb 4f 7 / 2 core level at 138.0 eV. None selected option as an escape depth
606 correction, was applied at each survey or high-resolution scan, before starting any further
607 quantification analysis.[61] For the compositional analysis of the core level spectra of I 3d 5 / 2, O 1s, C
608 1s and Pb 4f 7 / 2, the Scofield relative sensitivity factors of 16, 2.52, 1 and 13.7 were used,
609 respectively. The binding energy regions used for analysis, were kept constant with respect to each
610 element at each survey or high-resolution scan. Also, for each binding energy region, a Shirley type
611 background function was used.

612 **Rutherford back-scattering spectroscopy (RBS) measurements**. Two commercial and four
613 synthesised PbI_2 samples in the form of pellets with diameter ~ 13 mm and thickness ~1.5 mm, were
614 prepared using a press under an applied mass of 9 tons. For the RBS measurements, a 1.7 MV
615 Tandetron RBS linear type tandem ion beam accelerator was used, which is located in the Laboratory
616 of Ion Beam Physics at the ETH Zurich facilities in Switzerland. PbI_2 pellets were bombarded with
617 accelerated ions of $^4He^+$ at 2 MeV, while a PIN diode detector was placed at an angle of 168 °, in
618 respect to the beam of incident ions. The resulted data were plotted using the RUMP simulation
619 software.

620 **Atomic force microscopy (AFM) measurements**. Atomic force microscopy of the $CH_3NH_3PbI_3$ thin
621 films, was performed using a Dimension icon with ScanAsyst AFM (Bruker) with a cantilever
622 consisting of a silicon tip on a silicon nitride lever (Bruker) (f = 70 kHz, k = 0.4 N * m^{-1}).

623

624 **Supporting Information**

625 - Section 1 Discussion of polytypism in PbI_2

- SEM –EDS data
- Photograph of HT and MC PbI_2 samples, completed films, sample preparation and the vacuum assisted drying set-up
- XRD peak positons for different PbI_2 polytypes
- Section 2 XPS discussion and results
- RBS data and calculated stoichiometric ratios
- Percentage unreacted PbI_2 as determined from XRD
- Photograph of residual PbI_2 in perovskite microcrystal powder
- Microcrystal XRD data
- Section 3 description of method to determine stoichiometry from crystallization XRD
- Section 4 Iodine deficiency discussion including example calculations
- SEM images : Cross section SEM of SA and MC films, SA and MC microcrystals, film coverage for SA, MC, SA(microcrystal) and MC(microcrystal) films plus grain size distributions
- Device I(V) plots
- Tauc plots for SA and MC samples
- TRPL fitting parameters
- AFM images of SA and MC samples

Conflicts of interest

D. G. L. is a co-director of the company Ossila Ltd. that retail materials and equipment used in perovskite photovoltaic device research and development.

Acknowledgements

This work was funded by the UK Engineering and Physical Sciences Research Council (EPSRC) via a PhD studentship for K. Tsevas at the University of Sheffield from the Centre for Doctoral Training in New and Sustainable Photovoltaics, grant code EP/L01551X/1, which J. A. Smith also acknowledges for funding. A.D.F Dunbar wishes to acknowledge support from the EPSRC through Supergen Solar Challenge Grant: EP/M025020/1. C. Rodenburg and V. Kumar thank EPSRC for funding under grant EP/N008065/1. We appreciate the assistance from N. Reeves McLaren from the

University of Sheffield for providing the D2 Phaser (Bruker) X-ray diffractometer. We also appreciate the assistance from D. Hammond, who carried out the X-ray photoelectron spectroscopy measurements in Sheffield Surface Analysis Centre. K. Tsevas wishes to acknowledge the access provided through the RADIATE GATE scheme for RBS measurements, proposal number 19001741-ST. We also appreciate the assistance from Hans-Arno Synal, Christof Vockenhuber and colleagues from the Laboratory of Ion Beam Physics at the ETH Zurich facilities in Switzerland, who carried out the RBS measurements and analysis of PbI_2 samples. M. Vasilopoulou acknowledges support of this work by the project "Development of Materials and Devices for Industrial, Health, Environmental and Cultural Applications" (MIS 5002567), which is implemented under the "Action for the Strategic Development on the Research and Technological Sector", funded by the Operational Program "Competitiveness, Entrepreneurship and Innovation" (NSRF 2014-2020) and co-financed by Greece and the European Union (European Regional Development Fund).

References

(1) Kojima A., Teshima K., Shirai Y., Miyasaka T.. Organometal Halide Perovskites as Visible-Light Sensitizers for Photovoltaic Cells. *J. Am. Chem. Soc.,* **2009**, 131 (17), 6050–6051.

(2) Shin S.S., Yeom E.J., Yang W.S., Hur S., Kim M.G., Im J., Seo J., Noh J.H., Seok S.I.. Colloidally prepared La-doped $BaSnO_3$ electrodes for efficient, photostable perovskite solar cells. *Science,* **2017**, 356, 167–171.

(3) Wang R., Mujahid M., Duan Y., Wang Z., Xue J., Yang Y.. A Review of Perovskites Solar Cell Stability. *Adv. Funct. Mater.,* **2019**, 1808843, 1–25.

(4) Huang F., Li M., Siffalovic P., Cao G., Tian J.. From scalable solution fabrication of perovskite films towards commercialization of solar cells. *Energy Environ. Sci.* **2019**, 12, 518–549.

(5) Jacobsson T.J., Correa-Baena J.P., Halvani Anaraki E., Philippe B., Stranks S.D., Bouduban M.E.F., Tress W., Schenk K., Teuscher J., Moser J.E., Rensmo H., Hagfeldt A.. Unreacted PbI_2 as a Double-Edged Sword for Enhancing the Performance of Perovskite Solar Cells. *J. Am. Chem. Soc.,* **2016**, 138, 10331–10343.

681 (6) Saliba M., Matsui T., Seo J.Y., Domanski K., Correa-Baena J.P., Nazeeruddin M.K., Zakeeruddin
682 S.M., Tress W., Abate A., Hagfeldt A., Grätzel M.. Cesium-containing triple cation perovskite solar
683 cells: improved stability, reproducibility and high efficiency. *Energy Environ. Sci.,* **2016**, 9, 1989.
684 (7) Roose B., Dey K., Chiang Y.H., Friend R. H., Stranks S. D.. A critical assessment of the use of excess
685 lead iodide in lead halide perovskite solar cells. *J. Phys. Chem. Lett.* **2020**, 11, 16, 6505–6512.
686 (8) Song Z., Watthage S.C., Phillips A.B., Heben M.J.. Pathways toward high-performance perovskite
687 solar cells: review of recent advances in organo-metal halide perovskites for photovoltaic applications.
688 *J. of Photonics for Energy,* **2016**, 6 (2), 022001.
689 (9) Chang J., Zhu H., Li B., Isikgor F.H., Hao Y., Xu Q. Ouyang J.. Boosting the performance of planar
690 heterojunction perovskite solar cell by controlling the precursor purity of perovskite materials. *J. of*
691 *Mater. Chem. A,* **2016**, 4, 887–893.
692 (10) Yao J., Yang L., Cai F., Yan Y., Gurney R.S., Liu D., Wang T.. The impacts of PbI_2 purity on the
693 morphology and device performance of one-step spray-coated planar heterojunction perovskite solar
694 cells. *Sustain Energy and Fuels,* **2018**, 2, 436–443.
695 (11) Kumar V., Barbe J., Schmidt W.L., Tsevas K., Ozkan B., Handley C.M., Freeman C. L., Sinclair D.
696 C., Reaney I. M., Tsoi W. C., Dunbar A., Rodenburg C.. Stoichiometry-dependent local instability in
697 $MAPbI_3$ perovskite materials and devices. *J. of Mater. Chem. A.,* **2018**, 6, 23578–23586.
698 (12) Zhang Y., Lv H., Cui C., Xu L., Wang P., Wang H., Yu X., Xie J., Huang J., Tang Z., Yang D..
699 Enhanced optoelectronic quality of perovskite films with excess CH_3NH_3I for high-efficiency solar
700 cells in ambient air. *Nanotechnology,* **2017**, 28, 205401.
701 (13) Mastroianni S., Heinz F.D., Im J. H., Veurman W., Padilla M., Schubert M.C., Wurfel U., Grätzel M.,
702 Park N. G., Hinsch A.. Analysing the effect of crystal size and structure in highly efficient
703 $CH_3NH_3PbI_3$ perovskite solar cells by spatially resolved photo- and electroluminescence imaging.
704 *Nanoscale,* 2015, **7**, 19653–19662.
705 (14) Song Z., Watthage S.C., Phillips A.B., Tompkins B.L., Ellingson R.J., Heben M.J.. Impact of
706 Processing Temperature and Composition on the Formation of Methylammonium Lead Iodide
707 Perovskites. *Chem. of Mater.,* **2015**, 27(13), 4612–4619.
708 (15) Chen Z., Dong Q., Liu Y., Bao C., Fang Y., Lin Y., Tang S., Wang Q., Xiao X., Bai Y., Deng Y.,

Huang J.. Thin single crystal perovskite solar cells to harvest below-bandgap light absorption. *Nat. Commun.,* **2017**, 8, 1890.

(16) Yen H.J., Liang P.W., Chueh C.C., Yang Z., Jen A.K.Y., Wang H.L.. Large Grained Perovskite Solar Cells Derived from Single-Crystal Perovskite Powders with Enhanced Ambient Stability. *ACS Appl. Mater. and Interfaces,* **2016**, 8, 14513–14520.

(17) Ferreira Da Silva A., Veissid N., An C.Y., Pepe I., Barros De Oliveira N., Batista Da Silva A. V.. Optical determination of the direct bandgap energy of lead iodide crystals. *Appl. Phys. Lett.,* **1996**, 69, 1930–1932.

(18) Shah K.S., Olschner F., Moy L.P., Bennett P., Misra M., Zhang J., Squillante M.R., Lund J.C.. Lead iodide X-ray detection systems. *Nucl. Instruments Methods in Phys. Res. A.,* **1996**, 380, 266–270.

(19) Beckmann P.A.. A review of polytypism in lead iodide. *Cryst. Res. Technol.,* **2010**, 45, 455–460.

(20) Trigunayat G.C.. A survey of the phenomenon of polytypism in crystals. *Solid State Ionics,* **1991**, 48, 3–70.

(21) Palosz B., Steurer W., Schulz H.. The structure of PbI_2 polytypes 2H and 4H: a study of the 2H-4H transition. *J. of Phys. Condens. Matter.,* **1990**, 2, 5285–5295.

(22) Wei Q., Shen B., Chen Y., Xu B., Xia Y., Yin J., Liu Z., Large-sized PbI_2 single crystal grown by co-solvent method for visible-light photo-detector application. *Mater. Lett.,* **2017**, 193, 101–104.

(23) Patel A.R., Rao A.V.. An improved design to grow larger and more perfect single crystals in gels. *J. of Cryst. Growth,* **1980**, 49, 589–590.

(24) Street R.A., Ready S.E., Lemmi F., Shah K.S., Bennett P., Dmitriyev Y.. Electronic transport in polycrystalline Pbl_2 films. *J. of Appl. Phys.,* **1999**, 86, 2660–2667.

(25) Zheng Z., Liu A., Wang S., Wang Y., Li Z., Lau W.M., Zhang L.. In situ growth of epitaxial lead iodide films composed of hexagonal single crystals. *J. of Mater. Chem.,* **2005**, 15, 4555–4559.

(26) Zhu X.H., Wei Z.R., Jin Y.R., Xiang A.P.. Growth and characterization of a PbI_2 single crystal used for gamma ray detectors. *Cryst. Res. and Technol.,* **2007**, 42, 456–459.

(27) Hassan M.A., Jafar M.M., Matuchova M., Bulos B.N.. An experimental evidence of some lead iodide polytypes compatible with the dielectric functions model. J. of Appl. Sci., **2010**, 10, 3367–3373.

(28) Salje E., Palosz B., Wruck B.. In situ observation of the polytypic phase transition 2H-12R in PbI_2 :

investigations of the thermodynamic structural and dielectric properties. *J. of Phys. C: Solid State Phys.,* **1987**, 20, 4077–4096.

(29) Falk A.L., Buckley B.B., Calusine G., Koehl W.F., Dobrovitski V.V., Politi A., Zorman C. A., Feng P. X. L., Awschalom D. D.. Polytype control of spin qubits in silicon carbide. *Nat. Commun.,* **2013**, 4, 1–7.

(30) Li X., Bi D., Yi C., Decoppet J.D., Luo J., Zakeeruddin S.M., Hagfeldt A., Grätzel M.. A vacuum flash-assisted solution process for high-efficiency large-area perovskite solar cells. *Science,* **2016**; 353, 58–62.

(31) Wu C., Zhang Q., Liu Y., Luo W., Guo X., Huang Z., Ting H., Sun W., Zhong X., Wei S., Wang S., Chen Z., Xiao L.. The Dawn of Lead-Free Perovskite Solar Cell : Highly Stable Double Perovskite $Cs_2AgBiBr_6$ Film. *Adv. Sci.,* **2017**, 1700759, 2–9.

(32) Konstantakou M., Perganti D., Falaras P., Stergiopoulos T.. Anti-Solvent Crystallization Strategies for Highly Efficient Perovskite Solar Cells. *Crystals,* **2017**, **7**, 1-21.

(33) Bredig M.A., Bamberger C.E., Richardson D.M.. A mixed-valency lead oxyiodide. *J. of Inorg. Nucl. Chem.,* **1978**, 40, 1497–1500.

(34) Berry F.J., Jones C.H.W., Dombsky M.. An Iodine Mossbauer Study of Lead(II) Iodide and Lead Oxyiodide. *J. of Solid State Chem.,* **1983**, 46, 41–45.

(35) Tavakoli F., Salavati-Niasari M., Mohandes F.. Sonochemical Synthesis and Characterization of Lead Iodide Hydroxide Micro / nanostructures. *Ultrason. Sonochem.,* **2014**, 21, 234–241.

(36) Butyagin P.Y., Streletskii A.N.. The Kinetics and Energy Balance of Mechanochemical Transformations. *Phys. of Solid State,* **2005**, 47, 856–862.

(37) Wang S., Jiang Y., Juarez-Perez E.J., Ono L.K., Qi Y.. Accelerated degradation of methylammonium lead iodide perovskites induced by exposure to iodine vapour. *Nat. Energy,* **2016**, 2, 16195.

(38) Brenes R., Eames C., Bulović V., Islam M.S., Stranks S.D.. The Impact of Atmosphere on the Local Luminescence Properties of Metal Halide Perovskite Grains. *Adv. Mater.,* **2018**, 30, 1706208.

(39) Wang Q., Chen B., Liu Y., Deng Y., Bai Y., Dong Q., Huang J.. Scaling behavior of moisture-induced grain degradation in polycrystalline hybrid perovskite thin films. *Energy Environ. Sci.,* **2017**, 10, 516–522.

765 (40) Kim S., Bae S., Lee S.W., Cho K., Lee K.D., Park S., Kwon G., Ahn S.W., Lee H.M., Kang Y., Lee
766 H.S., Kim D.. Relationship between ion migration and interfacial degradation of $CH_3NH_3PbI_3$
767 perovskite solar cells under thermal conditions. *Sci. Rep.,* **2017**, **7**, 1200.
768 (41) Besleaga C., Abramiuc L.E., Stancu V., Tomulescu A.G., Sima M., Trinca L., Plugaru N., Pintilie L.,
769 Nemmes G.A., Iliescu M., Svavarsson H.G., Manolescu A., Pintilie I.. Iodine Migration and
770 Degradation of Perovskite Solar Cells Enhanced by Metallic Electrodes. *J. of Phys. Chem. Lett.,* **2016**,
771 **7**, 5168–5175.
772 (42) Wong-Stringer M., Game O.S., Smith J.A., Routledge T.J., Alqurashy B.A., Freestone B.G., Parnell
773 A.J., Vaenas N., Kumar V., Alawad M.O.A, Iraqi A., Rodenburg C., Lidzey D.G.. High-Performance
774 Multilayer Encapsulation for Perovskite Photovoltaics. *Adv. Energy Mater.,* **2018**, 8, 1801234.
775 (43) Acik M., Alam T.M., Guo F., Ren Y., Lee B., Rosenberg R.A., Mitchell J.F., Park I.K., Lee G.,
776 Darling S.B.. Substitutional Growth of Methylammonium Lead Iodide Perovskites in Alcohols. *Adv.*
777 *Energy Mater.,* **2018**, 8, 1701726.
778 (44) Heo J.H., Song D.H., Han H.J., Kim S.Y., Kim J.H., Kim D., Shin H.W., Ahn T.K., Wolf C., Lee
779 T.W., Im S.H.. Planar $CH_3NH_3PbI_3$ Perovskite Solar Cells with Constant 17.2% Average Power
780 Conversion Efficiency Irrespective of the Scan Rate. *Adv. Mater.,* **2015**, 27, 3424–3430.
781 (45) Rolda-Carmona C., Gratia P., Zimmermann I., Grancini G., Gao P., Graetzel M., Nazeeruddin M.K..
782 High efficiency methylammonium lead triiodide perovskite solar cells: the relevance of non-
783 stoichiometric precursors. *Energy Environ. Sci.,* **2015**, 8, 3550–3556.
784 (46) Jeon N.J., Noh J.H., Kim Y.C., Yang W.S., Ryu S., Seok S. Il.. Solvent engineering for high-
785 performance inorganic-organic hybrid perovskite solar cells. *Nat. Mater.,* **2014**, 13, 897–903.
786 (47) Xiao M., Huang F., Huang W., Dkhissi Y., Zhu Y., Etheridge J., Weale A.G., Bach U., Cheng Y.B.,
787 Spiccia L.. Perovskite Solar Cells Hot Paper A Fast Deposition-Crystallization Procedure for Highly
788 Efficient Lead Iodide Perovskite Thin-Film Solar Cells. *Angew. Chemie. Int. Ed* ., **2014**, 53, 9898–
789 9903.
790 (48) Ummadisingu A., Grätzel M.. Revealing the detailed path of sequential deposition for metal halide
791 perovskite formation. *Sci. Adv.,* **2018**, 4, e1701402.
792 (49) Philippe B., Saliba M., Correa-Baena J.P., Cappel U.B., Turren-Cruz S.H., Grätzel M., Hagfeldt A.,

Rensmo H.. Chemical Distribution of Multiple Cation (Rb^+, Cs^+, MA^+, and FA^+) Perovskite Materials by Photoelectron Spectroscopy. *Chem. of Mater.,* **2017**, 29, 3589–3596.

(50) Du T., Burgess C.H., Kim J., Zhang J., Durrant R., Mclachlan M.A.. Formation, location and beneficial role of PbI_2 in lead halide perovskite solar cells. *Sustain Energy and Fuels,* **2017**, 1, 119–126.

(51) Da Silva Filho J.M.C., Ermakov V.A., Marques F.C.. Perovskite Thin Film Synthesised from Sputtered Lead Sulphide. *Sci. Rep.,* **2018**, 8, 1563.

(52) Mayerhofer T., Popp J.. Beyond Beer's Law: Spectral Mixing Rules. Appl. Spectrosc., 2020, 74(10),1287-1294.

(53) Wang Q., Shao Y., Xie H., Lyu L., Liu X., Gao Y., Huang J.. Qualifying composition dependent p and n self-doping in $CH_3NH_3PbI_3$. *Appl. Phys. Lett.,* **2014**, 105, 163508.

(54) Cui P., Wei D., Ji J., Huang H., Jia E., Dou S., Wang T., Wang W., Li M.. Planar p–n homojunction perovskite solar cells with efficiency exceeding 21.3%. *Nat. Energy,* **2019**, 4(2), 150–159.

(55) Rothmann M.U., Li W., Zhu Y., Bach U., Spiccia L., Etheridge J., Cheng Y.B.. Direct observation of intrinsic twin domains in tetragonal $CH_3NH_3PbI_3$. *Nat. Commun.,* **2017**, 8, 14547.

(56) Liu Y., Collins L., Proksch R., Kim S., Watson B.R., Doughty B., Calhoun T.R., Ahmadi M., Levlev A.V., Jesse S., Retterer S.T., Belianinov A., Xiao K., Huang J., Sumpter B.G., Kalinin S.V., Hu B., Ovchinnikova O.S.. Chemical nature of ferroelastic twin domains in $CH_3NH_3PbI_3$ perovskite. *Nat. Mater.,* **2018**, 17, 1013–1019.

(57) Lan C., Zhou Z., Wei R., Ho J.C.. Two-dimensional perovskite materials: From synthesis to energy-related applications. *Mater. Today Energy,* **2019**, 11, 61–82.

(58) Kutes Y., Zhou Y., Bosse J.L., Steffes J., Padture N.P., Huey B.D.. Mapping the Photoresponse of $CH_3NH_3PbI_3$ Hybrid Perovskite Thin Films at the Nanoscale. *Nano Lett.,* **2016**, 16, 3434–3441.

(59) Jiang Q., Zhang L., Wang H., Yang X., Meng J., Liu H., Yin Z., Wu J., Zhang X., You J.. Enhanced electron extraction using SnO_2 for high-efficiency planar-structure $HC(NH_2)_2PbI_3$-based perovskite solar cells. *Nat. Energy,* **2016**, 2, 16177.

(60) Saliba M., Correa-Baena J.P., Wolff C.M., Stolterfoht M., Phung N., Albrecht S., Neher D., Abate A.. How to Make over 20% E ffi cient Perovskite Solar Cells in Regular (n−i−p) and Inverted (p−i−n)

Architectures. *Chem. Mater.,* **2018**, 30, 4193–4201.

(61) Powell C.J., Jablonski A.. Electron effective attenuation lengths for applications in Auger electron spectroscopy and x-ray photoelectron spectroscopy. *Surf. and Interface Anal.,* **2002**, 33, 211–229.

Table of Contents Graphic